SOLAR CELLS

Low trap-state density and long carrier diffusion in organolead trihalide perovskite single crystals

Dong Shi,[1]* Valerio Adinolfi,[2]* Riccardo Comin,[2] Mingjian Yuan,[2] Erkki Alarousu,[1] Andrei Buin,[2] Yin Chen,[1] Sjoerd Hoogland,[2] Alexander Rothenberger,[1] Khabiboulakh Katsiev,[1] Yaroslav Losovyj,[3] Xin Zhang,[4] Peter A. Dowben,[4] Omar F. Mohammed,[1] Edward H. Sargent,[2] Osman M. Bakr[1]†

The fundamental properties and ultimate performance limits of organolead trihalide MAPbX₃ (MA = CH₃NH₃⁺; X = Br⁻ or I⁻) perovskites remain obscured by extensive disorder in polycrystalline MAPbX₃ films. We report an antisolvent vapor-assisted crystallization approach that enables us to create sizable crack-free MAPbX₃ single crystals with volumes exceeding 100 cubic millimeters. These large single crystals enabled a detailed characterization of their optical and charge transport characteristics. We observed exceptionally low trap-state densities on the order of 10^9 to 10^{10} per cubic centimeter in MAPbX₃ single crystals (comparable to the best photovoltaic-quality silicon) and charge carrier diffusion lengths exceeding 10 micrometers. These results were validated with density functional theory calculations.

Solution-processed hybrid organolead trihalide (MAPbX₃) perovskite solar cells (PSCs) have now achieved 20.1% certified power conversion efficiencies (1), following a rapid surge of development since perovskite-based devices were first reported in 2009 (2). A key to the success of PSCs is the long diffusion length of charge carriers in the absorber perovskite layer (3). This parameter is expected to depend strongly on film crystallinity and morphology. Thermally evaporated MAPbI₃ films fabricated using a Cl⁻-based metal salt precursor were reported to exhibit carrier diffusion lengths three times those of the best solution-processed materials, yet no measurable Cl⁻ was incorporated in the final films, hinting at a major but unclear mechanism in the control of crystallinity and morphology (4, 5). These observations suggest that there may be room to improve upon already remarkable PSC efficiencies via the optimization of three key parameters: charge carrier lifetime, mobility, and diffusion length.

The quest for further improvements in these three figures of merit motivated our exploration of experimental strategies for the synthesis of large single-crystal MAPbX₃ perovskites that would exhibit phase purity and macroscopic (millimeter)

dimensions. Unfortunately, previously published methods failed to produce single crystals with macroscopic dimensions large enough to enable electrode deposition and practical characterization of electrical properties (6). Past efforts based on cooling-induced crystallization were hindered by (i) the limited extent to which solubility could be influenced by controlling temperature, (ii) the complications arising from temperature-dependent phase transitions in MAPbX₃, and (iii) the impact of convective currents (arising from thermal gradients in the growth solution) that disturb the ordered growth of the crystals.

We hypothesized that a strategy using antisolvent vapor-assisted crystallization (AVC), in which an appropriate antisolvent is slowly diffused into a solution containing the crystal precursors, could lead to the growth of sizable MAPbX₃ crystals of high quality (with crack-free, smooth surfaces, well-shaped borders, and clear bulk transparency). Prior attempts to grow hybrid perovskite crystals with AVC have fallen short of these qualities—a fact we tentatively attributed to the use of alcohols as antisolvents (7). Alcohols act as good solvents for the organic salt MAX (8) due to solvent-solute hydrogen bond interactions; as a result, they can solvate MA⁺ during the ionic assembly of the crystal, potentially disrupting long-range lattice order.

We instead implemented AVC (Fig. 1A) using a solvent with high solubility and moderate coordination for MAX and PbX₂ [N,N-dimethylformamide (DMF) or γ-butyrolactone (GBA)] and an antisolvent in which both perovskite precursors are completely insoluble [dichloromethane (DCM)]. We reasoned that DCM, unlike alcohols, is an extremely poor solvent for both

MAX and PbX₂ and lacks the ability to form hydrogen bonds, thus minimizing asymmetric interactions with the ions during their assembly into crystal form. When combined with a slow and controlled diffusion rate into DMF or GBA, our approach established the conditions for all the ionic building blocks of the perovskite to be coprecipitated from solution stoichiometrically.

Using this method, we grew high-quality, millimeter-sized MAPbBr₃ and MAPbI₃ single crystals (fig. S1) (9) whose shape conformed to the underlying symmetry of the crystal lattice. The phase purity of the as-grown crystals was confirmed by x-ray diffraction (XRD) performed on powder ground from a large batch of crystals (Fig. 1B).

The synthesized crystals were of sufficient quality and macroscopic dimensions to enable a detailed investigation of the optical and charge transport properties. The absorbance of MAPbX₃ (X = Br⁻ or I⁻) (Fig. 2) shows a clear band edge cutoff with no excitonic signature, which suggests a minimal number of in-gap defect states. For comparison, the absorption spectrum from the polycrystalline MAPbBr₃ (fig. S2) (9) and MAPbI₃ (5) thin films shows a peak near the band gap, which is often attributed to an excitonic transition. This observation is consistent with a substantial amount of disorder and lack of long-range structural coherence in nanostructured thin films (10). By extrapolating the linear region of the absorption edge to the energy-axis intercept (fig. S3) (9), we determined the optical band gaps of MAPbBr₃ and MAPbI₃ single
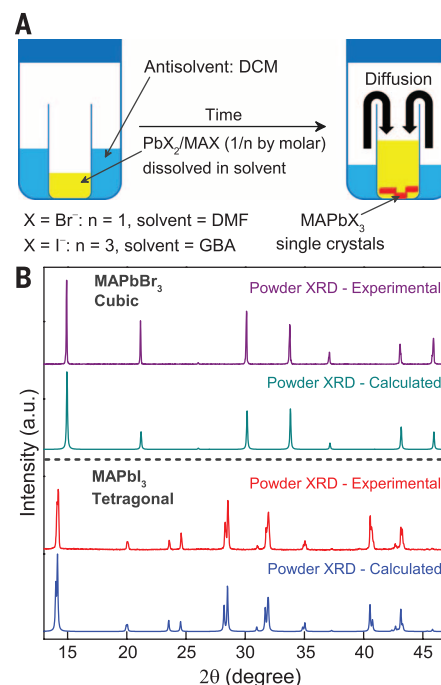

Fig. 1. Crystal growth and diffraction. (A) Schematic diagram of the crystallization process. (B) Experimental and calculated powder XRD profiles confirming the phase purity of MAPbX₃ crystals grown at room temperature (fig. S1). Single-crystal XRD data are given in (9).

[1]Solar and Photovoltaic Engineering Research Center (SPERC), King Abdullah University of Science and Technology (KAUST), 23955-6900 Thuwal, Saudi Arabia. [2]Department of Electrical and Computer Engineering, University of Toronto, Toronto, Ontario M5S 3G4, Canada. [3]Department of Chemistry, Indiana University, Bloomington, IN 47405, USA. [4]Department of Physics and Astronomy, University of Nebraska, Lincoln, NE 68588, USA. *These authors contributed equally to this work. †Corresponding author. E-mail: osman.bakr@kaust.edu.sa

crystals to be 2.21 and 1.51 eV (Fig. 2), respectively. Both materials in their single-crystalline form exhibit a substantially narrower band gap than the corresponding films, which could enhance photon harvesting and hence improve photocurrent generation.

As also shown in Fig. 2, both MAPbBr$_3$ and MAPbI$_3$ exhibit a narrow photoluminescence (PL) that peaks near the band edge. A noticeable

Fig. 2. Steady-state absorbance and photoluminescence.
(**A**) MAPbBr$_3$ single crystal.
(**B**) MAPbI$_3$ single crystal. Insets: Absorbance versus photon energy and the determined band gap Eg. PL excitation wavelength was 480 nm.
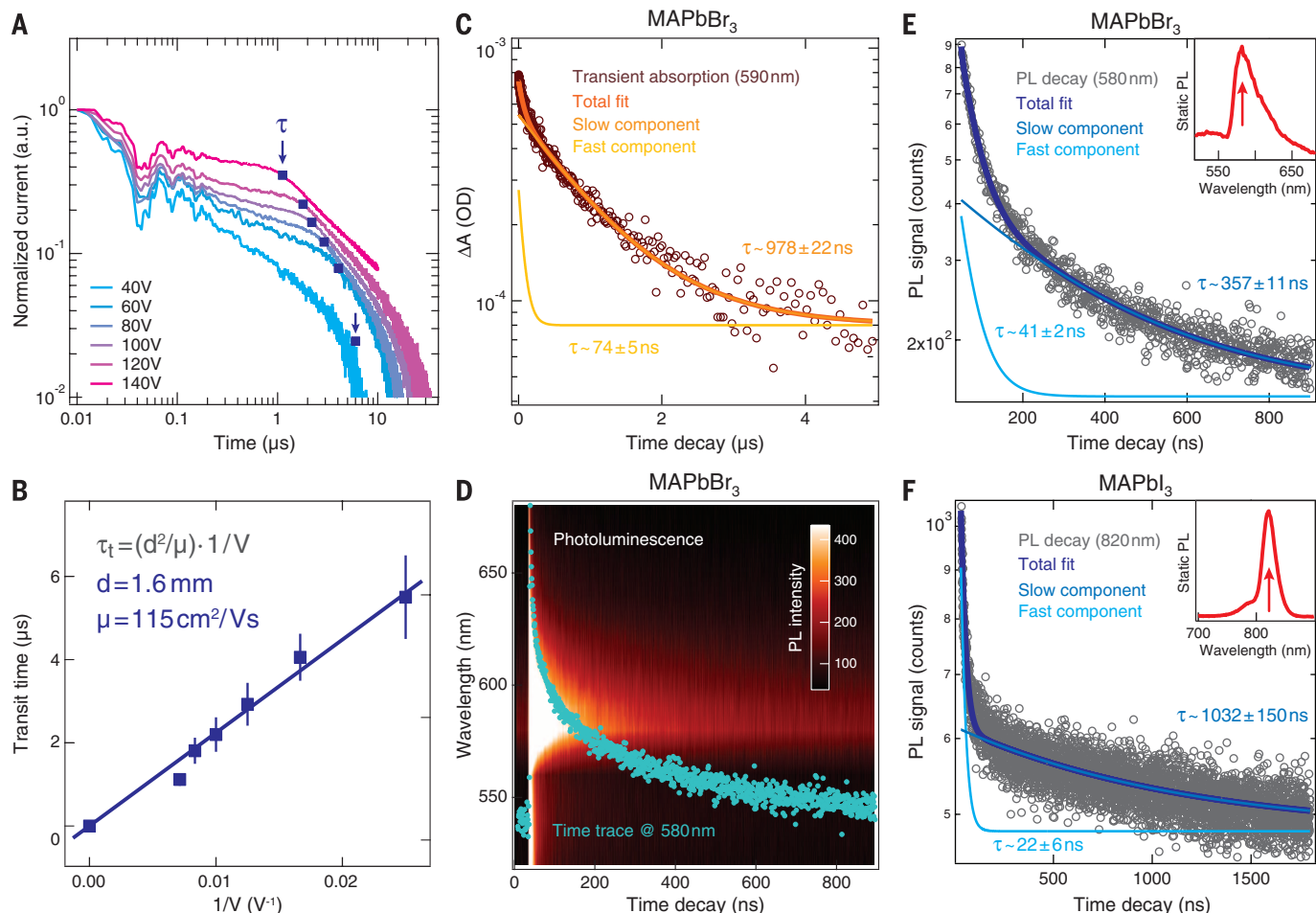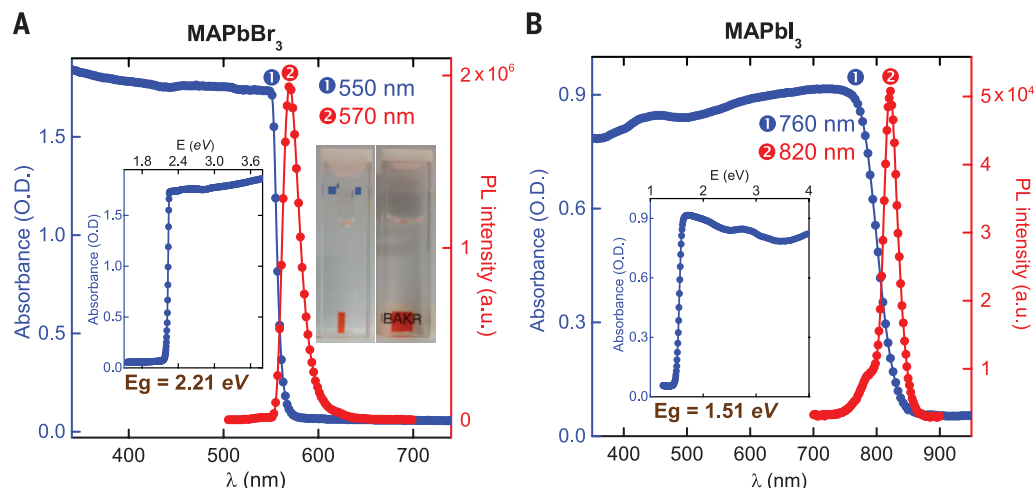

Fig. 3. Carrier mobility and lifetime measurements. (**A**) Time-of-flight traces showing the transient current after photoexcitation at time t = 0 in a bilogarithmic plot; the transit time τ$_t$ is identified by the corner in each trace and marked by blue squares. (**B**) Linear fit of transit time versus inverse voltage V^{-1}. (**C**) Transient absorption in MAPbBr$_3$ crystals, evaluated at 590 nm, showing a fast component (τ ≈ 74 ± 5 ns) together with a slower decay (τ ≈ 978 ± 22 ns). (**D**) Time- and wavelength-dependent photoluminescence (PL) color map, with the time trace at λ = 580 nm superimposed (blue markers). (**E**) PL time decay trace on a MAPbBr$_3$ crystal at λ = 580 nm, with biexponential fits showing a fast (τ ≈ 41 ± 2 ns) and a slow transient (τ ≈ 357 ± 11 ns). (**F**) PL time decay trace on a MAPbI$_3$ crystal (λ = 820 nm, also showing a fast (τ ≈ 22 ± 6 ns) and a slow (τ ≈ 1032 ± 150 ns) component.

shoulder at ~790 nm in the PL of MAPbI$_3$ single crystals is in agreement with the PL from thin films (5), with the main PL peaking at 820 nm attributed to the intrinsic PL from the MAPbI$_3$ crystal lattice. A more structured PL spectrum was observed for polycrystalline MAPbBr$_3$ thin films (fig. S2) (9).

We investigated the key quantities that directly affect a material's potential for application in PSCs: carrier lifetime τ, carrier mobility μ, and carrier diffusion length L_D. In addition, we estimated the in-gap trap density n_{traps} in order to correlate the trap density with the observed diffusion length. For MAPbBr$_3$ single crystals, we first measured carrier mobility using the time-of-flight technique (11). The transient current was measured for various driving voltages (V), and the corresponding traces are shown in Fig. 3A on a bilogarithmic scale. The transit time τ$_t$, defined as the position of the kink in the time traces, is marked by the blue squares, and the corresponding values are plotted in Fig. 3B as a function of V^{-1}. The mobility μ [μ = μ$_p$ ≈ μ$_n$, where μ$_p$ and μ$_n$ are the hole and electron mobility, respectively (12, 13)] can be directly estimated from the transit time τ$_t$, sample thickness d, and applied voltage V as μ = $d^2/V\tau_t$ (Fig. 3B) (9). Estimating mobility via a linear fit of τ$_t$ versus V^{-1} led to an estimate of 115 cm^2 V^{-1} s^{-1}. Complementary Hall effect measurements at room temperature confirmed a carrier (holes) concentration of between 5×10^9 and 5×10^{10} cm^{-3}, and provided a mobility estimate in the range from 20 to 60 cm^2 V^{-1} s^{-1}. Slightly lower mobilities obtained via the Hall effect may be ascribed to surface effects that are negligible for time-of-flight, which constitutes a bulk probe.

For MAPbI$_3$ single crystals, we estimated the carrier mobility using the space-charge-limited current (SCLC) technique. We measured the current-voltage (I-V) trace for the crystals and observed a region showing a clear quadratic dependency of the current on the applied voltage at 300 K (see fig. S8 for details). From this region, we could conservatively estimate the carrier mobility, obtaining the value μ = 2.5 cm^2 V^{-1} s^{-1}.

From the linear ohmic region, we also identified the conductivity of the crystal to be σ = 1 × 10^{-8} (ohm·cm)$^{-1}$. Combining the information on mobility and conductivity, we estimated a carrier concentration of n_c = σ/eμ ≈ 2 × 10^{10} cm^{-3} (where e is the electronic charge).

We estimated the carrier lifetime τ from transient absorption (TA) and PL spectra. Nanosecond pump-probe TA spectroscopy was carried out over a window covering the nanosecond-to-microsecond time scales in order to evaluate the fast (τ ≈ 74 ns) as well as the slow (τ ≈ 978 ns) carrier dynamics, as determined from biexponential fits. Time (t)– and wavelength (λ)–resolved PL maps IPP(t, λ) (Fig. 3D) of single-crystalline MAPbBr$_3$ were acquired in the wavelength region around the main band-to-band recombination peak at 580 nm (λ = 500 to 680 nm). The time-dependent PL signals in single-crystalline samples of MAPbBr$_3$ and MAPbI$_3$ are shown in Fig. 3, E and F, respectively; the data were measured at the wavelength of the main PL peak—i.e., λ = 580 nm and λ = 820 nm for MAPbBr$_3$ and MAPbI$_3$, respectively (see insets).

The time-resolved traces are representative of the transient evolution of the electron-hole population after impulsive (Δt ≈ 0.7 ns) photoexcitation. Biexponential fits were performed to quantify the carrier dynamics (fig. S4, blue traces) (9). Both the bromide- and iodide-based perovskite crystals exhibited a superposition of fast and slow dynamics: τ ≈ 41 and 357 ns for MAPbBr$_3$, and τ ≈ 22 and 1032 ns for MAPbI$_3$. We assign these two very different time scales to the presence of a surface component (fast) together with a bulk component (slow), which reveals the lifetime of carriers propagating deeper in the material. The relative contribution of these two terms to the static PL can be readily evaluated by integrating the respective exponential traces (the integral is equal to the product of the amplitude A and the decay time τ), which shows that the fast (tentatively surface) component amounts to only 3.6% of the total TA signal in MAPbBr$_3$, and to 12% and 7% of the total PL signal in MAPbBr$_3$ and MAPbI$_3$, respectively.

Ultimately, by combining the longer (bulk) carrier lifetimes with the higher measured bulk mobility, we obtained a best-case carrier diffusion length L_D = ($k_B T/e \cdot \mu \cdot \tau$)$^{1/2}$ (where k_B is Boltzmann's constant and T is the sample temperature) of ~17 μm in MAPbBr$_3$; use of the shorter lifetime and lower mobility led to an estimate of ~3 μm. The same considerations were applied for the MAPbI$_3$ crystals to obtain a best-case diffusion length of ~8 μm and a worst-case length of ~2 μm.

For comparison, we also investigated the PL decay of solution-processed thin films of MAPbBr$_3$ (fig. S5). We again found two dynamics: a fast decay (τ ≈ 13 ns) and a longer-lived component (τ ≈ 168 ns), in both cases faster than the single crystals. This result suggests a larger trap-induced recombination rate in the thin films, which are expected to possess a much higher trap density than the single crystals. Previous studies on non–Cl-doped MAPbI$_3$ nanostructured thin films also corroborate this trend, revealing a PL lifetime of ~10 ns and a carrier diffusion length of ~100 nm (3, 5).

Crystalline MAPbX$_3$ is characterized by a charge transport efficiency that outperforms thin film–based materials in mobility, lifetime, and diffusion length. To unveil the physical origins of this difference, we investigated the concentration of in-gap deep electronic trap states. We measured the I-V response of the crystals in the SCLC regime (Fig. 4). Three regions were evident in the experimental data. At low voltages, the I-V response was ohmic (i.e., linear), as confirmed by the fit to an I ≈ V functional dependence (blue line). At intermediate voltages, the current exhibited a rapid nonlinear rise (set in at V$_{TFL}$ = 4.6 V for MAPbBr$_3$ and 24.2 V for MAPbI$_3$) and signaled the transition onto the trap-filled limit (TFL)—a regime in which all the available trap states were filled by the injected carriers (14). The onset voltage V$_{TFL}$ is linearly proportional to the density of trap states n_{traps} (Fig. 4A). Correspondingly, we found for MAPbBr$_3$ single crystals a remarkably low trap density n_{traps} = 5.8×10^9 cm^{-3}, which, together with the extremely clean absorption and PL profiles (see again Fig. 2A), points to a nearly defect-free electronic structure. At high fields, the current showed a quadratic voltage dependence in the Child's regime. In this region, we extracted the value for the trap-free mobility μ. We found μ = 38 cm^2 V^{-1} s^{-1} (Fig. 4A), a value in good agreement with the mobility extracted using time-of-flight and Hall effect measurements (fig. S7) (9). We determined a comparable low trap density n_{traps} = 3.3×10^{10} cm^{-3} for MAPbI$_3$ single crystals using the same method (Fig. 4B).

The defect density measured for the room temperature–grown MAPbX$_3$ crystals was superior to a wide array of established and emerging optoelectronic inorganic semiconductors including polycrystalline Si (n_{traps} ≈ 10^{13} to 10^{14} cm^{-3}) (15, 16), CdTe/CdS (n_{traps} ≈ 10^{11} to 10^{13} cm^{-3}) (17), and copper indium gallium selenide (CIGS) (n_{traps} ≈ 10^{13} cm^{-3}) thin films (18), as well as organic materials such as single-crystal rubrene (n_{traps} ≈ 10^{16} cm^{-3}) (19) and pentacene (n_{traps} ≈ 10^{14} to 10^{15} cm^{-3}) (20). Only

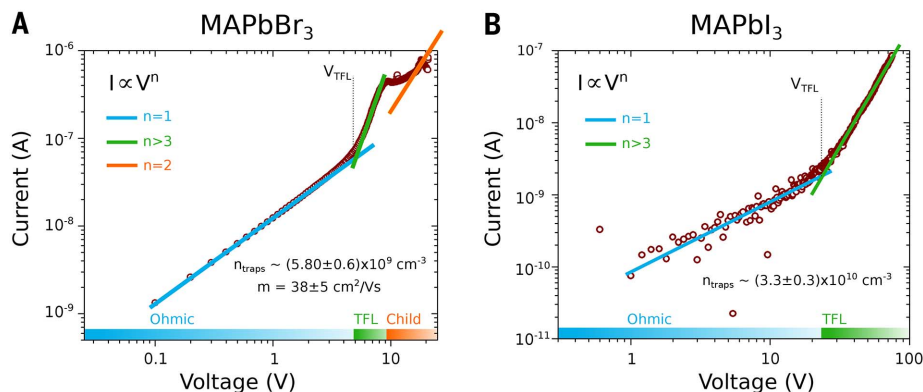**Fig. 4. Current-voltage traces and trap density.** Characteristic I-V trace (purple markers) showing three different regimes for (**A**) MAPbBr$_3$ (at 300 K) and (**B**) MAPbI$_3$ (at 225 K). A linear ohmic regime (I ∝ V, blue line) is followed by the trap-filled regime, marked by a steep increase in current (I ∝ V$^{n>3}$, green line). The MAPbBr$_3$ trace shows a trap-free Child's regime (I ∝ V^2, green line) at high voltages.

ultrahigh-quality crystalline silicon, grown at high temperatures, offers comparable or better deep trap densities ($10^8 < n_{traps} < 10^{15}$ cm^{-3}) (21, 22). The exceptionally low trap density found experimentally can be explained with the aid of density functional theory (DFT) calculations performed on MAPbBr$_3$, which predict a high formation energy for deep trap defects when MAPbBr$_3$ is synthesized under Br-rich conditions (e.g., from PbBr$_2$ and MABr), such as is the case in this study (9).

REFERENCES AND NOTES

1. National Renewable Energy Laboratory, Best Research-Cell Efficiencies; www.nrel.gov/ncpv/images/efficiency_chart.jpg.
2. A. Kojima, K. Teshima, Y. Shirai, T. Miyasaka, J. Am. Chem. Soc. **131**, 6050–6051 (2009).
3. T. C. Sum, N. Mathews, Energy Environ. Sci. **7**, 2518–2534 (2014).
4. C. Wehrenfennig, M. Liu, H. J. Snaith, M. B. Johnston, L. M. Herz, Energy Environ. Sci. **7**, 2269–2275 (2014).
5. S. D. Stranks et al., Science **342**, 341–344 (2013).
6. D. B. Mitzi, Prog. Inorg. Chem. **48**, 1–121 (1999).
7. Y. Tidhar et al., J. Am. Chem. Soc. **136**, 13249–13256 (2014).
8. M. Xiao et al., Angew. Chem. Int. Ed. **53**, 9898–9903 (2014).
9. See supplementary materials on Science Online.
10. J. J. Choi, X. Yang, Z. M. Norman, S. J. L. Billinge, J. S. Owen, Nano Lett. **14**, 127–133 (2014).
11. J. R. Haynes, W. Shockley, Phys. Rev. **81**, 835–843 (1951).
12. G. Giorgi, K. Yamashita, J. Mater. Chem. A 10.1039/C4TA05046K (2015).
13. E. Edri, S. Kirmayer, D. Cahen, G. Hodes, J. Phys. Chem. Lett. **4**, 897–902 (2013).
14. M. A. Lampert, P. Mark, Current Injection in Solids (Academic Press, New York, 1970).
15. J. R. Ayres, J. Appl. Phys. **74**, 1787–1792 (1993).
16. I. Capan, V. Borjanović, B. Pivac, Sol. Energy Mater. Sol. Cells **91**, 931–937 (2007).
17. A. Balcioglu, R. K. Ahrenkiel, F. Hasoon, J. Appl. Phys. **88**, 7175–7178 (2000).
18. L. L. Kerr et al., Solid-State Electron. **48**, 1579–1586 (2004).
19. C. Goldmann et al., J. Appl. Phys. **99**, 034507 (2006).
20. Y. S. Yang et al., Appl. Phys. Lett. **80**, 1595–1597 (2002).
21. J. R. Haynes, J. A. Hornbeck, Phys. Rev. **100**, 606–615 (1955).
22. J. A. Hornbeck, J. R. Haynes, Phys. Rev. **97**, 311–321 (1955).

SOLAR CELLS

High-efficiency solution-processed perovskite solar cells with millimeter-scale grains

Wanyi Nie,[1]* Hsinhan Tsai,[2]* Reza Asadpour,[3]† Jean-Christophe Blancon,[2]† Amanda J. Neukirch,[4,5] Gautam Gupta,[1] Jared J. Crochet,[2] Manish Chhowalla,[6] Sergei Tretiak,[4] Muhammad A. Alam,[3] Hsing-Lin Wang,[2]‡ Aditya D. Mohite[1]‡

State-of-the-art photovoltaics use high-purity, large-area, wafer-scale single-crystalline semiconductors grown by sophisticated, high-temperature crystal growth processes. We demonstrate a solution-based hot-casting technique to grow continuous, pinhole-free thin films of organometallic perovskites with millimeter-scale crystalline grains. We fabricated planar solar cells with efficiencies approaching 18%, with little cell-to-cell variability. The devices show hysteresis-free photovoltaic response, which had been a fundamental bottleneck for the stable operation of perovskite devices. Characterization and modeling attribute the improved performance to reduced bulk defects and improved charge carrier mobility in large-grain devices. We anticipate that this technique will lead the field toward synthesis of wafer-scale crystalline perovskites, necessary for the fabrication of high-efficiency solar cells, and will be applicable to several other material systems plagued by polydispersity, defects, and grain boundary recombination in solution-processed thin films.

T he recent discovery of organic-inorganic perovskites offers promising routes for the development of low-cost, solar-based clean global energy solutions for the future (1–4). Solution-processed organic-inorganic hybrid perovskite planar solar cells, such as CH$_3$NH$_3$PbX$_3$ (X = Cl, Br, I), have achieved high average power conversion efficiency (PCE) values of ~16% using a titania-based planar structure (1–7) or ~10 to 13% in the phenyl-C$_{61}$-butyric acid methyl ester (PCBM)–based architecture (8–10). Such high PCE values have been attributed to strong light absorption and weakly bound excitons that easily dissociate into free carriers with large diffusion length (11–13). The average efficiency is typically lower by 4 to 10% relative to the reported most efficient device, indicating persistent challenges of stability and reproducibility. Moreover, hysteresis during device operation, possibly due to defect-assisted trapping, has been identified as a critical roadblock to the commercial viability of perovskite photovoltaic technology (14–17). Therefore, recent efforts in the field have focused on improving film surface coverage (18) by increasing the crystal size and improving the crystalline quality of the grains (19), which is expected to reduce the overall bulk defect density and mitigate hysteresis by suppressing charge trapping during solar cell operation. Although approaches such as thermal annealing (20, 21), varying of precursor concentrations and carrier solvents (22), and using mixed solvents (23) have been investigated, control over structure, grain size, and degree of crystallinity remain key scientific challenges for the realization of high-performance devices.

Here, we report a solution-based hot-casting technique to achieve ~18% solar cell efficiency based on millimeter-scale crystalline grains, with relatively small variability (~2%) in the overall PCE from one solar cell to another. Figure 1A schematically describes our hot-casting process for deposition of organometallic perovskite thin films. Our approach involves casting a hot (~70°C) mixture of lead iodide (PbI$_2$) and methylamine hydrochloride (MACl) solution onto a substrate maintained at a temperature of up to 180°C and subsequently spin-coated (15 s) to obtain a uniform film (Fig. 1A). In the conventional scheme, the mixture of PbI$_2$ and MACl is spin-coated at room temperature and then post-annealed for 20 min on a hot plate maintained at 100°C. Figure 1, B to D, illustrates the obtained crystal grain structures using this hot-casting technique for various substrate temperatures and processing solvents. We chose a PbI$_2$/MACl molar ratio of 1:1 in all experiments described in this Report to achieve the basic perovskite composition and the best morphology (see fig. S1 for images). We observed large, millimeter-scale crystalline grains with a unique leaf-like pattern radiating from the center of the grain [see scanning electron microscopy (SEM) image of microstructure in fig. S2]. The x-ray diffraction (XRD) pattern shows sharp and strong perovskite (110) and (220) peaks for the hot-casted film, indicating a highly oriented crystal structure (fig. S3). The grain size increases markedly (Fig. 1, B and D) as the substrate temperature increases from room temperature up to 190°C or when using solvents with a higher boiling point, such

[1]Materials Physics and Application Division, Los Alamos National Laboratory, Los Alamos, NM 87545, USA. [2]Physical Chemistry and Applied Spectroscopy Division, Los Alamos National Laboratory, Los Alamos, NM 87545, USA. [3]School of Electrical and Computer Engineering, Purdue University, West Lafayette, IN 47907, USA. [4]Theoretical Chemistry and Molecular Physics Division, Los Alamos National Laboratory, Los Alamos, NM 87545, USA. [5]Center for Nonlinear Studies, Los Alamos National Laboratory, Los Alamos, NM 87545, USA. [6]Materials Science and Engineering, Rutgers University, Piscataway, NJ 08854, USA. *These authors contributed equally to this work. †These authors contributed equally to this work. ‡Corresponding author. E-mail: amohite@lanl.gov (A.D.M.); hwang@lanl.gov (H.-L.W.)